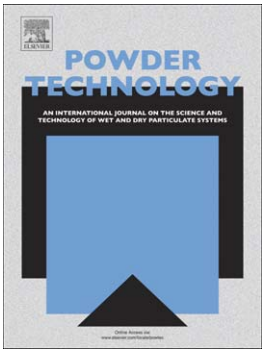

Effect of the synthesis conditions on the properties of $La_{0.15}Sm_{0.35}Sr_{0.08}Ba_{0.42}FeO_{3-\delta}$ cathode material for SOFCs

K. Vidal, A. Larrañaga, A. Morán-Ruiz, M.A. Laguna-Bercero, R.T. Baker, M.I. Arriortua

PII: S0032-5910(17)30742-8
DOI: doi:10.1016/j.powtec.2017.09.020
Reference: PTEC 12825

To appear in: *Powder Technology*

Received date: 16 May 2017
Revised date: 30 August 2017
Accepted date: 6 September 2017

Please cite this article as: K. Vidal, A. Larrañaga, A. Morán-Ruiz, M.A. Laguna-Bercero, R.T. Baker, M.I. Arriortua, Effect of the synthesis conditions on the properties of $La_{0.15}Sm_{0.35}Sr_{0.08}Ba_{0.42}FeO_{3-\delta}$ cathode material for SOFCs, *Powder Technology* (2017), doi:10.1016/j.powtec.2017.09.020

Effect of the synthesis conditions on the properties of $La_{0.15}Sm_{0.35}Sr_{0.08}Ba_{0.42}FeO_{3-\delta}$ cathode material for SOFCs

K. Vidal[a,*], A. Larrañaga[a], A. Morán-Ruiz[a], M.A. Laguna-Bercero[b], R.T. Baker[c] and M.I. Arriortua[a,*]

[a]Universidad del País Vasco (UPV/EHU), Facultad de Ciencia y Tecnología, Barrio Sarriena S/N, 48940 Leioa, Vizcaya, Spain.

[b] CSIC-Universidad de Zaragoza, Instituto de Ciencia de Materiales de Aragón (ICMA), Pedro Cerbuna 12, 50009 Zaragoza, Spain.

[c] EaStChem, School of Chemistry, University of St Andrews, St Andrews, Fife KY16 9ST, Scotland, United Kingdom.

Abstract:

The perovskite $La_{0.15}Sm_{0.35}Sr_{0.08}Ba_{0.42}FeO_{3-\delta}$ has been prepared by the glycine nitrate (GNC) route, varying the fuel/oxidizer ratio (glycine/nitrate, G/N= 1 and 2) and cooling rate (slow cooling and air-quenched), in order to study the influence of sample preparation on the materials' properties, in the context of their application as a cathode material for SOFCs. For this, the performance of the prepared mixed ion and electron conducting perovskite oxides is dictated by their structure, oxygen stoichiometry (3-δ), chemical composition and thermal expansion properties. High-resolution Synchrotron X-ray powder diffraction patterns were collected at room temperature and at 700 and 800ºC. It was found that the materials had a cubic crystal structure at these temperatures. As expected, 3-δ decreased as temperature increased, and was slightly smaller for the quenched sample. Higher electrical conductivity values were obtained for the sample with G/N = 1 (air-quenched) in the cooling rate. At 700 and 800°C the cathode synthesized with G/N = 1 and air-quenched showed the smallest polarization

resistance values in impedance spectroscopy studies. Therefore, the physicochemical and electrochemical characterization clearly demonstrated the influence of the synthetic conditions on the cathode performance.

Keywords: Chemical synthesis; Oxygen content; Cathode material; SOFC; Impedance Spectroscopy.

---

* Corresponding Author: Karmele Vidal and María Isabel Arriortua
e-mail: karmele.vidal@ehu.es and maribel.arriortua@ehu.es
Phone number: 946015984; Fax number: 946013500.

1. Introduction

Major obstacles to the commercialisation of solid oxide fuel cells are the limited long-term stability and high production costs. Both are related to the high operating temperatures of SOFC systems. The reason why high temperatures are nevertheless required is the general sluggishness of the kinetics of the elementary processes involved, most of which are thermally activated. A prominent example is the oxygen reduction reaction at the cathode, which is often the main limiting factor to the performance of the whole SOFC system [1]. One important goal in SOFC research is therefore the search for cathode materials which offer a sufficient electrochemical performance at intermediate temperatures (500-750ºC). One strategy to improve the cathode performance below 800ºC is to use mixed ionic-electronic conductors (MIECs) such as $(A_{1-x}Sr_x)(B)O_{3-\delta}$ (with A = Ba or La; B = Mn, Fe or Co). The possibility to transport oxygen ions and electrons through a single-phase material would extend the number of active sites for the oxygen reduction reaction (ORR) and enhance the cathode performance [2]. This doping strategy has been extensively applied to tailor the properties of perovskite oxides for various functional applications, including oxygen reduction electrodes for SOFCs [3].

Synthesis procedure and conditions can strongly affect the properties of perovskites, in particular of doped perovskites. Wet-chemical solution-combustion synthesis is an effective and economical approach [4]. The exothermicity of the reaction, which influences the powder characteristics such as crystallite size, surface area, phase purity and the nature of agglomeration, can be changed by varying the fuel to oxidant ratio and/or employing different fuels [5].

The simplest approach to account for variations of physical properties with A-site composition in these cathode materials is to consider a quasi-random distribution of

hard sphere cations over the A type sites. This has traditionally been parameterised through the average A cation radius $<r_A>$, often expressed as the Goldschmidt tolerance factor $t= (<r_A>+r_O) /\sqrt{2}(r_B+r_O)$ [6], where r_B and r_O are the B-site cation and oxide ion radii, respectively. A strong $<r_A>$ dependence of the electrochemical properties has been reported [7-9]. However, it was subsequently shown that a general description requires the use of an additional parameter, the A cation size disorder, which takes into account the inherent disorder due to the size mismatch between different cations occupying the A-site. This parameter has been quantified as the variance of the A cation radius distribution, $\sigma^2(r_A)=<r_A^2>-<r_A>^2$ [10].

Our group has studied the effect of this last parameter by impedance spectroscopy and a significant decrease in polarization resistance (Rp) with the application of the current was observed for a perovskite compound with a high value of $\sigma^2(r_A)$ [11,12].

It is well known that the performance of MIEC perovskite oxides is dictated by the structure, oxygen non-stoichiometry (δ), chemical composition and thermal expansion properties. In order to be able to track the oxygen vacancies with temperature, high-resolution Synchrotron X-ray powder diffraction (SXRPD) or neutron diffraction patterns are required.

Considering these objectives, this work focused on the synthesis of different $La_{0.15}Sm_{0.35}Sr_{0.08}Ba_{0.42}FeO_{3-\delta}$ compositions phases with high values of A cation size disorder ($\sigma^2(r_A)= 0.0231$ Å^2) obtained varying the fuel/oxidizer ratio and the cooling rate. The resulting compounds were characterized by X-ray powder diffraction (XRD), inductively coupled plasma atomic emission spectroscopy (ICP-AES), high-resolution Synchrotron X-ray powder diffraction (SXRPD), scanning electron microscopy (SEM), particle size distribution, electrical conductivity, I–V measurements and impedance spectroscopy.

2. Experimental

2.1. Powder preparation

$La_{0.15}Sm_{0.35}Sr_{0.08}Ba_{0.42}FeO_{3-\delta}$ samples were prepared by the glycine nitrate combustion (GNC) process, a self-combustion technique that uses glycine as fuel and nitrates of the metal components as oxidants.

The synthesis of the samples was performed using $La(NO_3)_3.6H_2O$ (>99%), $Sm(NO_3)_3.6H_2O$ (>99%), $Sr(NO_3)_2$. (>99.99%), $Ba(NO_3)_2$ (>99.995%), $Fe(NO_3)_2.9H_2O$ (98.5%) and glycine (>99%), all from Aldrich. The reagents were dissolved in distilled water and mixed in a 1 litre glass beaker, which was placed on a hot plate, under constant stirring, to evaporate excess water. The resulting viscous liquid started autoignition just after the glass beaker was placed directly onto a hotplate preheated at 450°C. The resulting powders were pelletized and calcined in air at 850, 1050 and 1250ºC for 10 h at each temperature to obtain the pure samples. Two samples were synthesised: one with the molar fuel/oxidizer ratio, G/N = 1 and a second with G/N=2. In addition, after the calcination at 1250ºC the first sample was cooled rapidly by air-quenching (at about 50ºC/min) and the second was cooled slowly (at 3ºC/min).

2.2. Characterization techniques

The structural analysis was performed using laboratory X-ray diffraction (XRD). Data were collected at room temperature (r.t.) using a Philips X'Pert-PRO X-ray diffractometer with secondary beam graphite monochromated Cu–Kα radiation, from 2θ 15 to 90°, with a step size of 0.026° and 10 s per step. The crystal structures were refined by the Rietveld method [13] using the GSAS software package [14].

Compositional analysis was performed on the prepared samples to confirm that the expected elemental composition was achieved. All metal contents were determined by

inductively coupled plasma atomic emission spectroscopy (ICP-AES) on a Horiba Yobin Yvon Activa spectrophotometer.

For both samples, *in situ* synchrotron powder diffraction data (ALBA, BL04-MSPD, the Spanish Synchrotron Radiation Facility, Barcelona) were collected in Debye-Scherrer (transmission) mode with a wavelength of 0.35 Å from room temperature up to 800 ºC in air. In addition, for the quenched sample, data were recorded during subsequent cooling to room temperature. The data acquisition time was ~2.5 h per pattern and this allowed a very good signal-to-noise ratio to be obtained over the angular range 2θ = 20-40°. SXRPD patterns were analysed using the Rietveld methodology as implemented in the GSAS software package.

The total electrical conductivity was measured in air from room temperature to 950°C using a heating rate of 3°C/min in air by applying a current of 0, 10, 50 and 100 mA using the four-point method on sintered rectangular bars of both perovskite samples. Electrical contacts were made using Pt wires and Pt paste placed over whole end faces ensuring a homogeneous current flow. The conductivity (σ) was determined from a set of V–I values by taking $\sigma=1/\rho=L/A\times dI/dV$, where L is the distance between voltage contacts and A is the sample cross section.

Prior to cell fabrication for the electrochemical tests, the compounds were ball milled under identical conditions for 24 h and particle sizes were measured using a Malvern Mastersizer X particle size analyser.

The impedance spectra were obtained using three-electrode configuration cells (Figure 1). The powders used as the working electrode were deposited on yttria stabilized zirconia (8YSZ) electrolyte disks (150 μm thick, Fuel Cell Materials) by wet

colloidal spraying (a total active area of 1 cm^2) followed by sintering at 1050°C for 2 h. Pt paste and mesh (Heraeus) were employed as the counter and the reference electrode.

(Figure 1)

The Pt reference electrode was painted on the same side as the working electrode, and care was taken to leave as large a distance as possible between the reference and working electrodes in order to minimize systematic errors in the measurement of the electrochemical characteristics. A Pt counter-electrode, having the same shape and position as the working electrode, was painted on the opposite side of the electrolyte pellet. Reference and counter electrodes were fixed to the electrolyte using a sintering treatment at 950ºC for 30 min.

AC impedance spectra were obtained using a Solartron 1260 Frequency Response Analyzer coupled to a Solartron 1286 electrochemical interface, with an applied voltage amplitude of 10 mV over a frequency range of 0.01 Hz to 1 MHz at measurement temperatures of 700 and 800°C (typical operating temperatures for the application of these materials in SOFC technology).

The morphologies of the powders and the sintered bars were examined using a scanning electron microscope (JEOL JSM-7000F). Secondary electron images were taken at 20 kV and $1.1.10^{-11}$ A.

3. Results and discussion

3.1. Structural Study

X-ray diffraction patterns collected for both $La_{0.15}Sm_{0.35}Sr_{0.08}Ba_{0.42}FeO_{3-\delta}$ samples are presented in Fig. 2 and showed that single-phase materials had been obtained without impurities.

(Figure 2)

Results from chemical analyses of the prepared powers are presented in Table 1 and show a good agreement with the expected nominal compositions.

(Table 1)

Figure 3 gives the raw SXRPD patterns, Rietveld fits and difference patterns for the quenched sample with G/N = 1 at 30, 700 and 800ºC (heating), and then at 700 and 30ºC on cooling.

(Figure 3)

Figure 4 shows raw SXRPD patterns, Rietveld fits and difference patterns for the slow cooled sample with G/N = 2 at 30, 700 and 800ºC.

(Figure 4)

Over the whole temperature range studied (25-800ºC), the SXRPD patterns for both samples were refined in a cubic symmetry (S.G: Pm-3m).

Final refined values of the structural parameters for the compounds are summarised in Tables 2 and 3.

(Table 2)

(Table 3)

Figures 5 and 6 show the evolution of the cell parameters and cell volume, and the average Fe-O, Fe-A and A-O bond distances obtained from the SXRPD data as a function of temperature.

(Figure 5)

(Figure 6)

As observed, all of these parameters increased on increasing the temperature. For the quenched sample, the structural parameters are slightly larger during heating than during cooling. However, there is a significant difference in the cell parameters between the samples prepared using different G/N ratios. At room temperature and 700ºC on heating, the values for G/N=1 (quenched) are significantly higher than for G/N=2 (slow-cooled), although they became very similar at 800ºC.

Figure 7 shows the oxygen stoichiometry for the samples determined from the structural refinements.

(Figure 7)

Setting aside the expected general thermal lattice expansion caused by increasing the temperature, the larger additional expansion observed for the G/N=1 (quenched) sample at r.t. and at 700°C on heating than in the subsequent cooling regime could be explained by the lower oxygen occupancy of the former (see Figure 7), which would lead to stronger repulsion between neighbouring cations and/or to an increased tendency to form the larger iron cation [15-17], Fe^{3+} (ionic radii are: Fe^{3+}(VI)= 0.645 Å; Fe^{4+}(VI)= 0.585 Å) [18]. Heating at 800°C allowed the oxygen occupancy to increase (equilibrate) and caused the lattice expansion at 700°C and r.t. to be smaller on cooling than on heating.

The smaller structural parameters for the sample with G/N = 2, could be explained because an increase of the fuel/oxidant ratio gives rise to changes in the perovskite structure, varying the oxygen vacancy concentration. This phenomenon was reported to result in a decrease in mean ionic radius of the B site ions (formation of Fe^{4+} cations) [19]. It is interesting that oxygen occupancy values for the two materials – like the other structural parameters – become very similar at 800ºC and this is attributed to the equilibration of oxygen vacancy concentration in both samples at this temperature.

3.2. Morphological study

Representative SEM micrographs of the powder samples synthesised by the glycine nitrate combustion method under the two conditions are shown in Figure 8. As observed, no significant differences can be seen in the morphology or the average particle size of the two samples in these images. Both samples are composed of agglomerated sub-micron particles.

(Figure 8)

The aggregation rate is determined by the temperature generated during the combustion reaction which is higher in the fuel-rich case. As has been reported in other works, the agglomerates formed at lower G/N ratio are soft and could be easily split up, while those at the higher ratio are hard and difficult to break into particles [5].

In Figure 9 the particle size distribution of unmilled and milled powders is shown.

(Figure 9)

The largest peak just below 1 μm is attributed to the presence of primary particles while those at higher particle sizes indicate the presence of agglomerates in the suspensions, in agreement with SEM observations. The G/N = 1 sample has a smaller fraction of agglomerates than the G/N=2 sample and has an average diameter (d_{50}) of 0.963 μm compared to 1.685 μm for G/N = 2. For both samples, the milling leads to a substantial decrease in mean particle size and in the presence of agglomerates, the d_{50} values being 0.710 and 0.830 μm for G/N = 1 and 2, respectively.

SEM micrographs taken of the surface of the sintered at 1250ºC bars are shown in Figure 10.

(Figure 10)

The observed microstructures present similar morphology with grain sizes from ~ 0.6 to 1.7 μm.

An agglomerate is defined as a limited arrangement of primary particles, which forms a network of interconnected pores. Weak agglomerates can be destroyed during compaction at relatively low pressures, so that inter- and intra-agglomerate pores of the same size with a narrow pore size distribution can be formed in such a powder. On the contrary, powders consisting of hard agglomerates cannot be compacted to give such a homogeneous pore size distribution which results in a decrease in sinterability [20].

In this work, this effect has been observed since relative densities of 88 and 83 % of the theoretical value (obtained by XRD) were obtained for the samples using G/N = 1 and 2, respectively. These results are in good agreement with the particle size distribution curves which show that fewer agglomerates were formed for G/N = 1 than for G/N = 2.

3.3. Electrical conductivity study

The total electrical conductivity measured by the four-point method as a function of temperature is shown in Figure 11 for the samples. As can be seen, the electrical conductivity of each specimen increased with increasing temperature up to a maximum value (at T_{max}) and then decreased. This indicates a transition in electrical conduction from (p-type) semiconducting to metallic, typical of perovskite-type mixed conductors [21]. The conductivity of the samples can be described by the small polaron conductivity model. In this model, the electronic conductivity is a result of the hopping of electrons from the occupied sites, Fe^{3+} ions, to the unoccupied sites, Fe^{4+} ions (electronic hole charge carriers in p-type semiconductors) [22]. It can be assumed that the behavior at low temperatures (where $\delta \sim 0$) reflects a thermally activated conduction mechanism and the electrical conductivity increases due to the increasing mobility of the electronic charge carriers. At high temperatures, the electronic conductivity is affected by the decrease in the number of p-type charge carriers due to progressive formation of oxygen vacancies [23,24].

(Figure 11)

The electrical conductivity values obtained at 700 and 800ºC (typical operating temperatures for the application of these materials in SOFC technology) by applying a current of 0, 10, 50 and 100 mA for the compounds are given in Table 4.

(Table 4)

The electrical conductivities obtained are comparable with those previously reported for this type of perovskite material with high $\sigma^2(r_A)$ values [7,11]. However, in this study, a slight decrease in electrical conductivity was observed for the sample with G/N = 2 when a current of 100 mA was applied. This is an interesting phenomenon that we have not found to be reported in the literature for similar compounds on varying the fuel to oxidant ratio in the synthesis procedure.

For the values obtained it can be concluded that the preparation route has an important influence on the electrical properties of these materials. The highest electrical conductivity was obtained for the sample with G/N = 1 during cooling. This behavior can be attributed to two factors: first, to the lower oxygen vacancy concentration on cooling than on heating (for the quenched sample) and applying a current of 100 mA (for the sampled with G/N = 2), given that, at high concentrations, oxygen vacancies can act as electron traps, decreasing the mobility of the carriers and so decreasing the electrical conductivity [25]; and secondly to the higher relative density for G/N = 1 than G/N = 2.

3.4. Electrochemical characterization

Electrochemical cells with the configuration $La_{0.15}Sm_{0.35}Sr_{0.08}Ba_{0.42}FeO_{3-\delta}$/YSZ/Pt were investigated using Impedance Spectroscopy (IS) under open circuit conditions and applying a cathodic current of 50 and 75 mA. The measurements were carried out in air at 700 and 800ºC during the heating step for both samples and at 700ºC during the cooling step for the quenched sample.

The typical Nyquist plots obtained for the samples are shown in Figure 12. The best fitting results were achieved with an equivalent circuit of $R_{ohm}(R_{HF}CPE_{HF})(R_{LF}CPE_{LF})$ as shown in Figure 12, indicating that at least two different electrode processes -

assigned to the high (HF) and low (LF) frequency arcs - are active; the oxygen reduction reaction at the electrode interface involves at least two different processes. In this equivalent circuit, R_{ohm}, is the overall ohmic resistance (including the electrolyte resistance and the resistance of the lead wires) which has been subtracted for clarity of the Nyquist plots; R_{HF} and R_{LF} are the polarization resistances of the high frequency and low frequency arcs (attributed to the polarization resistance, R_P, of the cathode reaction), respectively; and CPE_{HF} and CPE_{LF} are the corresponding constant phase elements.

(Figure 12)

The R_{HF} is attributed to the charge transfer processes involving oxygen ions at the electrode/electrolyte interface, and R_{LF} is related to the oxygen species adsorption-dissociation and diffusion phenomena on the electrode [26].

In Table 5 are reported the capacitance values for the electrode processes and the total polarization resistance ($Rp = R_{HF} + R_{LF}$) for both samples. The lower value of the capacitance C_{HF} (~10^{-4} $F.cm^{-2}$) indicates that this process is related to oxygen ion transfer and electronic processes, and the larger value of the capacitance C_{LF} (~10^{-2} $F.cm^{-2}$) can be related to molecular oxygen dissociation and diffusion process [27].

(Table 5)

It is observed that Rp decreases when increasing the temperature and is much smaller for the sample with G/N = 1. For this sample, it was also observed that Rp is slightly smaller on increasing (than on decreasing) the temperature, since the sample presents more oxygen vacancies and thus increasing the ionic conductivity [26,28]. This implies

that it is beneficial to apply "quenching" in the preparation of the cathode material in order to get lower Rp values.

The cross-sectional microstructures have been studied by SEM, showing similar microstructures and grain sizes. However, as shown above, the particles are more agglomerated in the sample with G/N=2 than for the G/N=1 one (Figure 9). This effect may have worsened the behaviour of the former sample, given that increased agglomeration would decrease the specific electrochemical surface area and the surface area available for adsorption/desorption processes, which, in turn, would increase Rp.

As have been studied for similar compositions with high values of $\sigma^2(r_A)$ [11,12], the Rp values are very sensitive to changes in applied currents. Figure 13 shows the typical Nyquist diagram of the impedance spectroscopy for Samples with G/N = 1 and 2 at 800°C at OCP and under a current of 50 and 100 mA. The Warburg impedance (W_1) in the equivalent circuit is related to the resistance of oxygen adsorption/decomposition and the oxygen ions diffusion in the cathode.

(Figure 13)

Table 6 shows the resistance and capacitance values at high and low frequency for the samples at 800ºC at OCP and under a current of 50 and 100 mA.

(Table 6)

It is interesting that a significant decrease in Rp is observed for both samples when applying a cathodic current, the decrease being greater for the cathode with G/N = 2, so strongly mitigating the effects of G/N ratio (Figure 13). This behaviour is in good

agreement with results obtained from conductivity measurements, showing a greater influence of the applied current on the electrochemical measurements for the cathode with G/N = 2.

To our knowledge, this is the first time that such an effect of the G/N value has resulted in significant cathode activation under different applied currents.

4. Conclusions

$La_{0.15}Sm_{0.35}Sr_{0.08}Ba_{0.42}FeO_{3-\delta}$ compounds have been obtained using a glycine-nitrate method by varying the fuel/oxidizer ratio (G/N = 1 and 2) and changing the cooling rate for the sample with G/N = 1 in order to study the effect of these factors on the structural, morphological and electrical properties of the materials. The SXRPD patterns for both samples, over the whole temperature range studied (30-800ºC), show cubic symmetry (S.G: Pm-3m). On cooling, the compound with a stoichiometric ratio (G/N = 1) value presented the highest values of electrical conductivity in the cooling step and showed the lowest value of Rp in the heating step in impedance measurements. When a current is applied, a significant decrease of this resistance is observed for the sample with G/N = 2. The Rp of the quenched sample with G/N = 1 showed less decrease of the polarization when applying current remaining similar than for the unquenched sample. Therefore, it can be concluded that the glycine-nitrate process, with a G/N ratio of 1 and applying “quenching”, is a more appropriate technique for preparing a promising candidate cathode for IT-SOFC applications.

Acknowledgements

This research has been funded by the Ministerio de Economía, Industria y Competitividad (MAT2016-76739-R (AEI/FEDER, UE) and MAT2015-86078-R), and

Departamento de Educación of the Basque Government (IT-630-13). The authors thank SGIker of UPV/EHU for technical and personnel support. This work was benefited from the BL04-MSPD beamline at ALBA. The authors thank Dr. Francois Fauth of the Experiments Division of ALBA for his assistance in situ synchrotron measurements. K. Vidal thanks UPV/EHU for funding.

5. References

[1] A.V. Berenov, A. Atkinson, J.A. Kilner, E. Bucher, W. Sitte, Oxygen tracer diffusion and surface exchange kinetics in $La_{0.6}Sr_{0.4}CoO_{3-\delta}$, Solid State Ionics 181 (2010) 819-826.

[2] S. Vazquez, L. Suescun, R. Faccio, Effect of Cu doping on $Ba_{0.5}Sr_{0.5}Fe_{1-x}Cu_xO_{3-\delta}$ perovskites for solid oxide fuel cells: A first-principles study, J. Power Sources 311 (2016) 13-20.

[3] Y. Chen, B. Qian, Z. Shao, Tin and iron co-doping strategy for developing active and stable oxygen reduction catalysts from $SrCoO_{3-\delta}$ for operating below 800°C, J. Power Sources 294 (2015) 339-346.[4] A. Bedon, M.M. Natile, A. Glisenti, On the synthesis and stability of $La_{0.6}Sr_{0.4}Ga_{0.3}Fe_{0.7}O_3$, J. Eur. Ceram. Soc. 37 (2017) 1049-1058.

[5] A.P. Jamale, S. Shanmugam, C.H. Bhosale, L.D. Jadhav, Physicochemical properties of combustion synthesized $La_{0.6}Sr_{0.4}Co_{0.8}Fe_{0.2}O_{3-\delta}$ perovskite: A role of fuel to oxidant ratio, Mat. Sci. Semicon. Proc. 40 (2015) 855-860.

[6] V.M. Goldschmidt, Skr. Norsk. Videnk.-Akad, Geochemische Verteilungsgesetze der Elemente, Mat. Nat. Kl. 2 (1926) and 8 (1927).

[7] A. Ecija, K. Vidal, A. Larrañaga, A. Martínez-Amesti, L. Ortega-San-Martín, M.I. Arriortua, Characterization of $Ln_{0.5}M_{0.5}FeO_{3-\delta}$ (Ln = La, Nd, Sm; M = Ba, Sr) perovskites as SOFC cathodes, Solid State Ionics 201 (2011) 35-41.

[8] X. Ding, X. Gao, W. Zhu, J. Wang, J. Jiang, Electrode redox properties of $Ba_{1-x}La_xFeO_{3-\delta}$ as cobalt free cathode materials for intermediate-temperature SOFCs, Int. J. Hydrog. Energ. 39 (2014) 12092-12100.

[9] K. Vidal, L. M. Rodríguez-Martínez, L. Ortega-San-Martín, M. L. Nó, T. Rojo, M. I. Arriortua, $Ln_{0.5}M_{0.5}FeO_{3-\delta}$ perovskites as cathode for solid oxide fuel cells: Effect

of mean radius of the A-Site cations, J. Electrochem. Soc. 157 (8) A919-A924 (2010).

[10] L.M. Rodríguez-Martínez, J.P. Attfield, Cation disorder and size effects in magnetoresistive manganese oxide perovskites, Phys. Rev. B. 54 (2002) R15622-R15625.

[11] K. Vidal, L.M. Martínez, L. Ortega-San-Martín, M.L. Nó, T. Rojo, M.I. Arriortua, Effect of the A cation size disorder on the properties of an iron perovskite series for their use as cathodes for SOFCs, Fuel Cells 11 (2011) 51-58.

[12] A. Ecija, K. Vidal, A. Larrañaga, A. Martínez-Amesti, L. Ortega-San-Martín , M.I. Arriortua, Structure and properties of perovskites for SOFC cathodes as a function of the A-site cation size disorder, Solid State Ionics 235 (2013) 14-21.

[13] J. Rodrıguez-Carvajal, FULLPROF Rietveld pattern matching analysis of powder patterns, Grenoble, 2011.

[14] A.C. Larson, R.B. Von Dreele, GSAS: general structure analysis system, LAUR; 1994.

[15] E. Lay, M. Benamira, C. Pirovano, G. Gauthier, L. Dessemond, Effect of Ce-doping on the electrical and electrocatalytical behavior of La/Sr chromo-manganite perovskite as new SOFC anode, Fuel Cells 12 (2012) 265-274.

[16] Y. Sun, N. Yan, J. Li, H. Wu, J.L. Luo, K.T. Chuang, The effect of calcination temperature on the electrochemical properties of $La_{0.3}Sr_{0.7}Fe_{0.7}Cr_{0.3}O_{3-x}$ (LSFC) perovskite oxide anode of solid oxide fuel cells (SOFCs). Sustain. Energy Technol. Assess. 8 (2014) 92-98.

[17] L. Ge, Z. Zhu, Z. Shao, S. Wang, S. Liu, Effects of preparation methods on the oxygen nonstoichiometry, B-site cation valences and catalytic efficiency of perovskite $La_{0.6}Sr_{0.4}Co_{0.2}Fe_{0.8}O_{3-\delta}$, Ceram. Int. 35 (2009) 3201-3206.

[18] R. D. Shannon, Revised effective ionic radii and systematic studies of interatomic distances in halides and calcogenides, Acta Cryst. A32 (1976) 751-767.

[19] F. Deganello, G. Marcí, G. Deganello, Citrate-nitrate auto-combustion synthesis of perovskite-type nanopowders: A systematic approach, J. Eur. Ceram. Soc. 29 (2009) 439-450.

[20] J. Majling, P. Znasik, V. Khandl, S. Komarneni, Porosimeter as a means to measure the compatibility of powders, J. Am. Ceram. Soc. 77 (1994) 1369-1371.

[21] L.W. Tai, M.M. Nasrallah, H.U. Anderson, D.M. Sparlin, S.R. Sehlin, Structure and electrical properties of $La_{1-x}Sr_xCo_{1-y}Fe_yO_3$. Part 1. The system $La_{0.8}Sr_{0.2}Co_{1-y}Fe_yO_3$, Solid State Ionics, 76 (1995) 259-271.

[22] P.A. Cox, The electronic structure and chemistry of solids, oxford science Publications, Oxford, UK, 1987.

[23] E. Bucher, W. Sitte, Defect chemical analysis of the electronic conductivity of strontium-substituted lanthanum ferrite, Solid State Ionics 173 (2004) 23-28.

[24] M. Chen, S. Paulson, V. Thangadurai, V. Birss, Sr-rich chromium ferrites as symmetrical solid oxide fuel cell electrodes, J. Power Sources 236 (2013) 68-79.

[25] H.H. Yu, X. Li, Z.G. Yuan, Synthesis and characterization hollow spherical $La_{0.7}Sr_{0.2}Ca_{0.1}Co_{0.9}Fe_{0.1}O_{3-\delta}$ (LSCCT) for cathode of solid state oxide fuel cell (SOFC), Metalurgija 22 (2016) 796-798.

[26] S.B. Alder, Limitations of charge-transfer models for mixed-conducting oxygen electrodes, Solid State Ionics 135 (2000) 603-612.

[27] M.J. Escudero, A. Aguadero, J.A. Alonso, L. Daza, A kinetic study of oxygen reduction reaction on La_2NiO_4 cathodes by means of impedance spectroscopy, J. Electroanal. Chem. 611 (2007) 107-116.

[28] J. Meng, N. Yuan, X. Liu, C. Yao, F. Meng, X. Niu, X. Wu, J. Meng, Assessment

of $LaM_{0.25}Mn_{0.75}O_{3-\delta}$ (M = Fe, Co, Ni, Cu) as promising cathode materials for intermediate-temperature solid oxide fuel cells, Electrochim. Acta 169 (2015) 264-275.

Figure Captions

Fig. 1. Schematic diagram of three-electrode configuration on YSZ electrolyte pellet.

Fig. 2. X-ray diffraction patterns for $La_{0.15}Sm_{0.35}Sr_{0.08}Ba_{0.42}FeO_{3-\delta}$ perovskites prepared by the glycine nitrate combustion method under different synthetic conditions.

Fig. 3. Rietveld refinement of the SXRPD patterns of quenched sample with G/N = 1 during a heating and cooling cycle in air.

Fig. 4. Rietveld refinement of the SXRPD patterns for the slow-cooled sample with G/N = 2 during heating in air at room temperature, 700 and 800ºC.

Fig. 5. Lattice parameters (a) and unit cell volumes (V) of $La_{0.15}Sm_{0.35}Sr_{0.08}Ba_{0.42}FeO_{3-\delta}$ samples at different temperatures (error bars are smaller than the used symbols).

Fig. 6. Average Fe-O, Fe-A and O-A bond distances for $La_{0.15}Sm_{0.35}Sr_{0.08}Ba_{0.42}FeO_{3-\delta}$ samples at different temperatures (error bars are smaller than the used symbols).

Fig. 7. Oxygen stoichiometry *vs* temperature of $La_{0.15}Sm_{0.35}Sr_{0.08}Ba_{0.42}FeO_{3-\delta}$ samples.

Fig. 8. Micrographs of $La_{0.15}Sm_{0.35}Sr_{0.08}Ba_{0.42}FeO_{3-\delta}$ perovskites obtained under two synthetic conditions.

Fig. 9. Particle size distribution of samples before (left) and after (right) milling.

Fig. 10. SEM micrographs taken of the surface of the sintered bars.

Fig. 11. Conductivity dependence upon temperature for the perovskites measured in air.

Fig. 12. Impedance spectra of cathodes measured: (a) at 700ºC during the heating and cooling steps for both samples and (b) at 800ºC for both samples.

Fig. 13. Impedance spectra of cathodes with: (a) G/N = 1 and (b) G/N = 2 measured at 800ºC and at OCP and with applied currents of 50 and 100 mA.

Tables

Table 1. Summary of the stoichiometric compositions obtained from ICP analyses for the perovskite products with nominal composition $La_{0.15}Sm_{0.35}Sr_{0.08}Ba_{0.42}FeO_{3-\delta}$.

Sample	La	Sm	Sr	Ba	Fe
G/N = 1 with "quenching"	0.13(1)	0.33(2)	0.07(2)	0.42(2)	1.00(3)
G/N = 2	0.15(2)	0.34(2)	0.07(2)	0.41(1)	1.00(3)

Table 2. Structural parameters obtained by Rietveld refinement for ABO_3 (A= $La_{0.15}Sm_{0.35}Sr_{0.08}Ba_{0.42}$; B= Fe) perovskite sintered by glycine nitrate combustion method with G/N = 1 at different temperatures.

T(ºC)	25	700	800	700	25
Symmetry	Cubic	Cubic	Cubic	Cubic	Cubic
Space group	Pm-3m	Pm-3m	Pm-3m	Pm-3m	Pm-3m
a (Å)	3.519103(3)	3.555759(5)	3.562199(6)	3.555754(5)	3.518974(9)
V/Z (Å^3)	43.581(1)	44.957(1)	45.202(1)	44.957(1)	43.576(1)
$\rho_{the.}$(g/cm^3)	9.166	8.963	8.692	8.834	9.199
A x=y=z	0.5	0.5	0.5	0.5	0.5
Uiso(x100 Å^2)	1.82(1)	3.30(2)	3.47(3)	3.25(2)	1.811(8)
Overall $Sm_{occup.}$	0.349(3)	0.353(6)	0.343(7)	0.348(6)	0.350(3)
Overall $La_{occup.}$	0.149(3)	0.153(6)	0.143(7)	0.148(6)	0.150(3)
Overall Sr_{occup}	0.079(3)	0.083(6)	0.073(7)	0.078(6)	0.080(3)
Overall Ba_{occup}	0.419(3)	0.423(6)	0.413(7)	0.418(6)	0.420(3)
B x=y=z	0	0	0	0	0
Uiso(x100 Å^2)	1.18(1)	2.24(3)	2.42(4)	2.24(3)	1.18(1)
Overall $Fe_{occup.}$	0.999(3)	1.003(6)	0.993(7)	0.997(6)	1.000(3)
O x	0.5	0.5	0.5	0.5	0.5
O y=z	0	0	0	0	0
Uiso(x100 Å^2)	3.8(1)	5.5(1)	5.5(2)	5.4(1)	3.8 (1)
Overall $O_{occup.}$	0.985(3)	0.973(6)	0.973(7)	0.977(6)	0.990 (3)
A-B (x12) (Å)	3.04763(1)	3.07938(1)	3.08495(1)	3.07937(1)	3.04752(1)
A-O (x12) (Å)	2.48838(1)	2.51430(1)	2.51886(1)	2.51430(1)	2.48829(1)
B-O (x6) (Å)	1.75955(1)	1.77788(1)	1.78110(1)	1.77788(1)	1.75949(1)
R_{wp} (%)	8.09	3.73	4.12	4.09	8.60
R_p (%)	6.53	3.52	4.14	4.08	7.11
χ^2	1.87	1.43	1.46	1.47	1.92

Table 3. Structural parameters obtained by Rietveld refinement for ABO_3 (A= $La_{0.15}Sm_{0.35}Sr_{0.08}Ba_{0.42}$; B= Fe) perovskite sintered by glycine nitrate combustion method with G/N = 2 at the temperatures indicated.

T(ºC)	25	700	800
Symmetry	Cubic	Cubic	Cubic
Space group	Pm-3m	Pm-3m	Pm-3m
a (Å)	3.51434(1)	3.549815(4)	3.562199(6)
V/Z (Å^3)	43.404(1)	44.732(1)	45.202(1)
$\rho_{the.}$(g/cm^3)	9.205	8.990	8.787
A x=y=z	0.5	0.5	0.5
Uiso(x100 Å^2)	1.800(7)	3.28(2)	3.49(3)
Overall $Sm_{occup.}$	0.348(2)	0.352(5)	0.347(7)
Overall $La_{occup.}$	0.148(2)	0.152(6)	0.147(7)
Overall Sr_{occup}	0.078(2)	0.082(5)	0.077(7)
Overall Ba_{occup}	0.418(2)	0.422(5)	0.417(7)
B x=y=z	0	0	0
Uiso(x100 Å^2)	1.17(1)	2.17(3)	2.39 (4)
Overall $Fe_{occup.}$	0.999(2)	1.002(5)	0.997(7)
O x	0.5	0.5	0.5
O y=z	0	0	0
Uiso(x100 Å^2)	4.6 (1)	5.7(1)	5.6(1)
Overall $O_{occup.}$	0.989(2)	0.975(5)	0.973(7)
A-B (x12) (Å)	3.04351(1)	3.07423(1)	3.08495(1)
A-O (x12) (Å)	2.48501(1)	2.51010(1)	2.51886(1)
B-O (x6) (Å)	1.75717(1)	1.77491(1)	1.78110(1)
R_{wp} (%)	6.78	3.29	4.56
R_p (%)	5.45	3.13	4.57
χ^2	1.65	1.32	1.52

Table 4. Electrical conductivity values of $La_{0.15}Sm_{0.35}Sr_{0.08}Ba_{0.42}FeO_{3-\delta}$ perovskites at 700 and 800ºC.

sample	σ_{Max} (S.cm^{-1})	σ(700ºC) (S.cm^{-1})	σ (800ºC) (S.cm^{-1})
G/N = 1, quenching (increasing T) 0, 50, 100 mA	22.90 (at 450ºC)	19.47	16.56
G/N = 1, quenching (decreasing T) 0, 50, 100 mA	27.13 (at 380ºC)	19.47	16.68
G/N = 2 0, 50 mA	20.43 (at 425ºC)	16.28	14.21
G/N = 2 100 mA	19.94 (at 427ºC)	15.89	13.57

Table 5. High frequency, low frequency and total polarization resistances and capacitances of the samples at 700 and 800ºC in air obtained by equivalent circuit fitting of the impedance spectra.

Sample	700ºC			800ºC		
	R_{HF} ($\Omega.cm^2$)	R_{LF} ($\Omega.cm^2$)	R_P ($\Omega.cm^2$)	R_{HF} ($\Omega.cm^2$)	R_{LF} ($\Omega.cm^2$)	R_P ($\Omega.cm^2$)
G/N = 1, "quenching" (increasing T)	6.89	6.42	13.31	1.35	0.95	2.30
G/N = 1, "quenching" (decreasing T)	10.54	10.14	20.68			
G/N = 2 (increasing T)	26.94	37.04	63.98	3.73	4.70	8.43
G/N = 2 (decreasing T)	28.37	40.21	68.58			
Sample	C_{HF} ($F.cm^2$)	C_{LF} ($F.cm^2$)		C_{HF} ($F.cm^2$)	C_{LF} ($F.cm^2$)	
G/N = 1, "quenching" (increasing T)	$5.3.10^{-5}$	$1.6.10^{-3}$		$4.9.10^{-5}$	$1.8.10^{-3}$	
G/N = 1, "quenching" (decreasing T)	$4.8.10^{-5}$	$1.9.10^{-3}$				
G/N = 2 (increasing T)	$6.1.10^{-5}$	$1.2.10^{-3}$		$6.2.10^{-5}$	$1.3.10^{-3}$	
G/N = 2 (decreasing T)	$5.9.10^{-5}$	$1.3.10^{-3}$				

Table 6. Electrode resistances and capacitances of the samples at 800ºC in air obtained by equivalent circuit fitting of the impedance spectra.

Resistance ($\Omega.cm^2$)	G/N = 1, "quenching"			G/N = 2		
	OCP	50 mA	100 mA	OCP	50 mA	100 mA
R_{HF}	1.35	1.12	0.80	3.73	1.26	0.68
R_{LF}	0.95	3.45	3.52	4.70	3.12	3.12
R_P	2.30	4.57	4.32	8.43	4.38	3.80
Capacitance ($F.cm^2$)	**OCP**	**50 mA**	**100 mA**	**OPC**	**50 mA**	**100 mA**
C_{HF}	$4.9.10^{-5}$	$4.5.10^{-4}$	$1.5.10^{-4}$	$6.2.10^{-5}$	$4.5.10^{-4}$	$9.3.10^{-4}$
C_{LF}	$1.8.10^{-3}$	$2.4.10^{-2}$	$2.7.10^{-3}$	$1.3.10^{-3}$	$2.4.10^{-2}$	$4.0.10^{-4}$

Figure 1

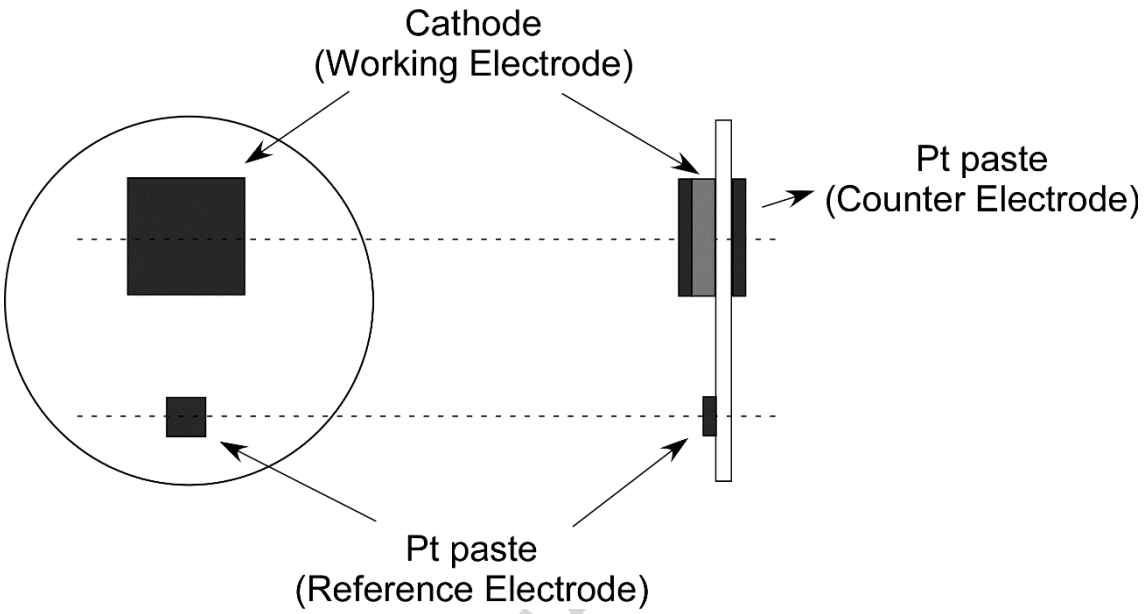

Figure 2

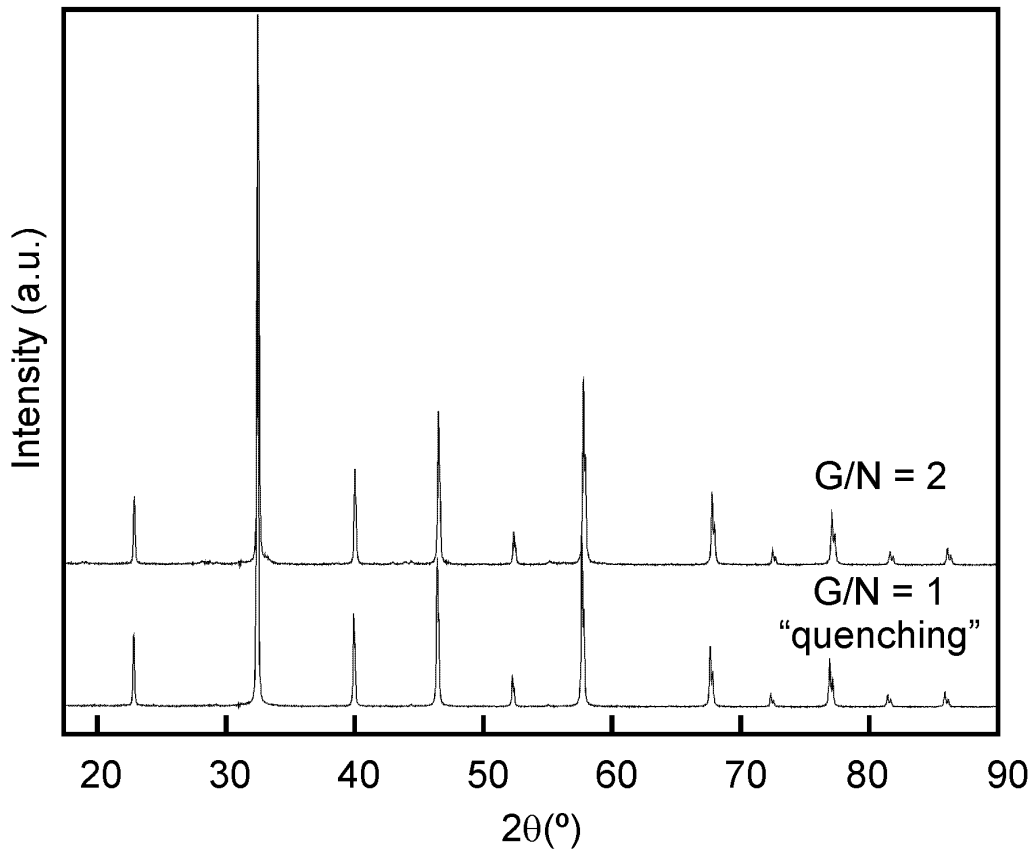

Figure 3

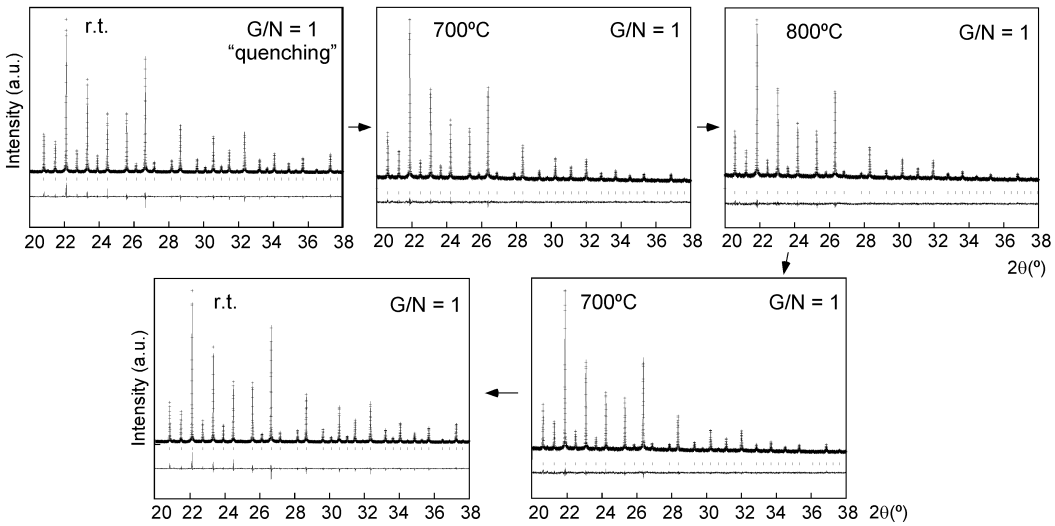

Figure 4

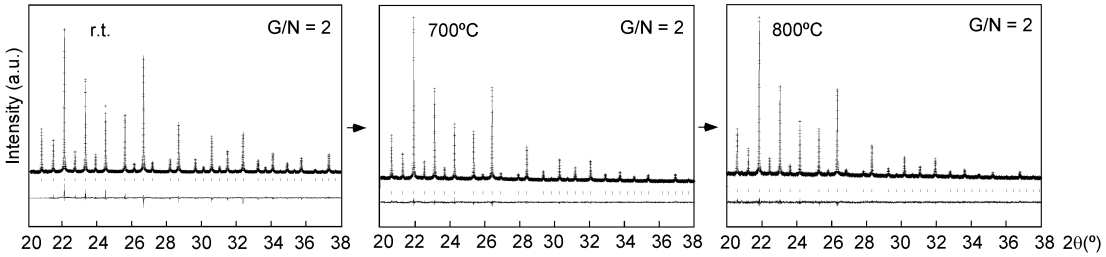

Figure 5

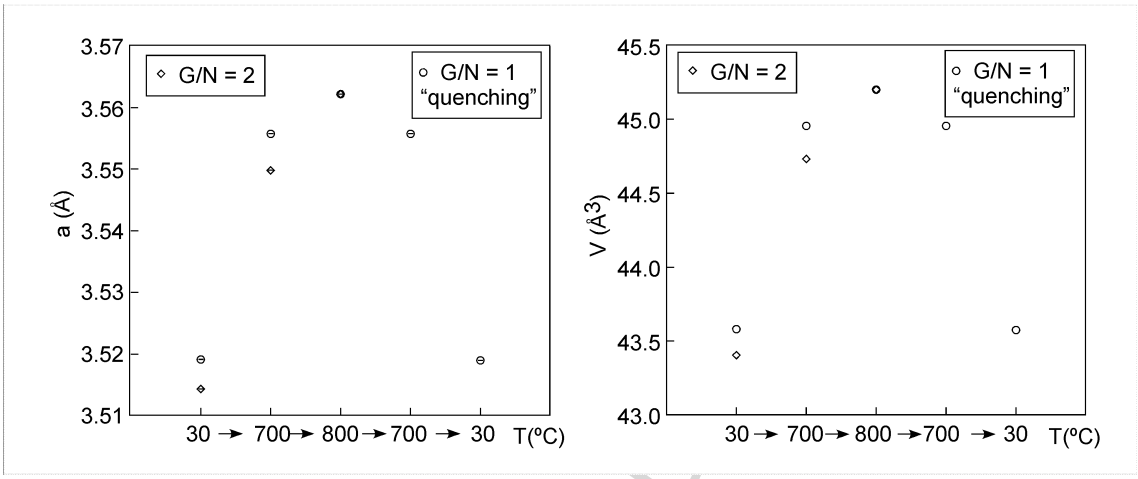

Figure 6

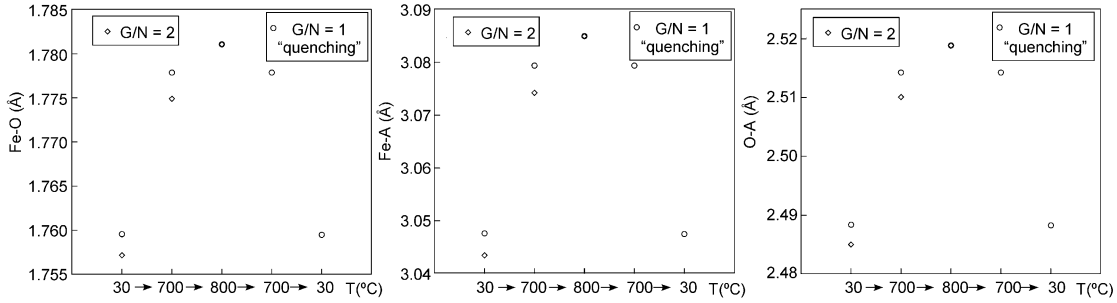

Figure 7

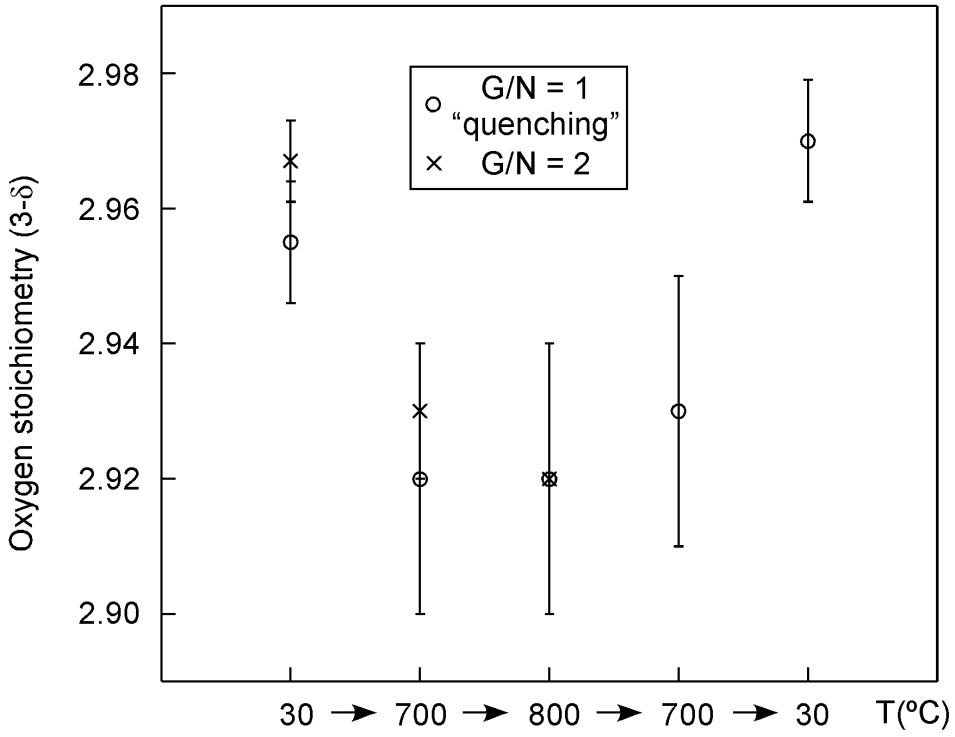

Figure 8

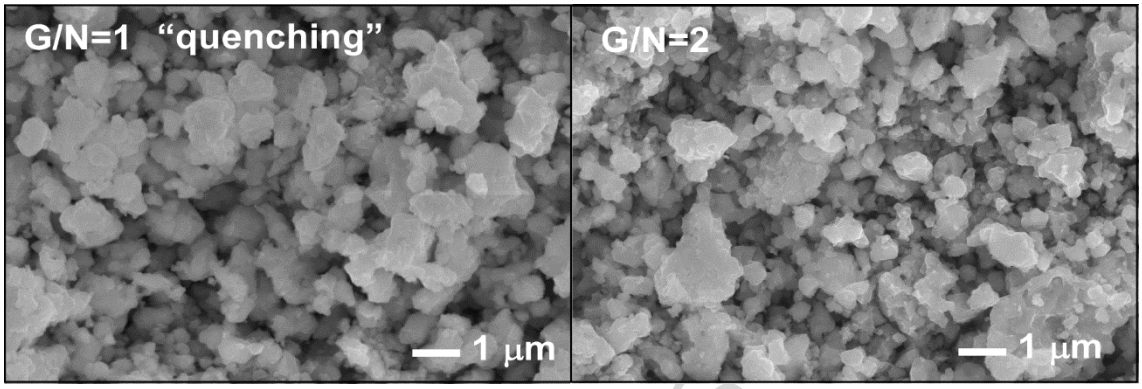

Figure 9

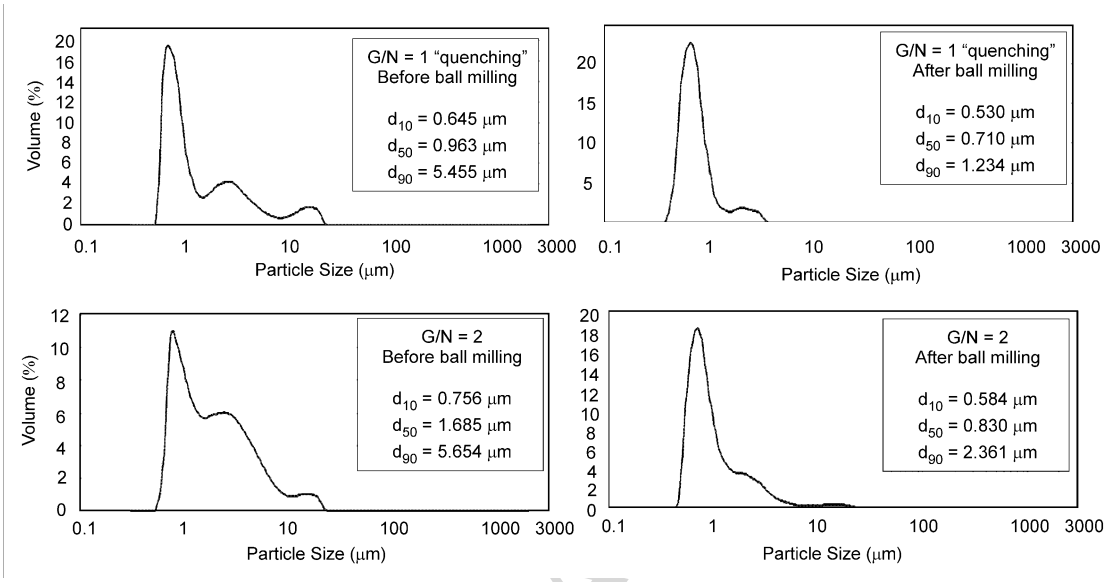

Figure 10

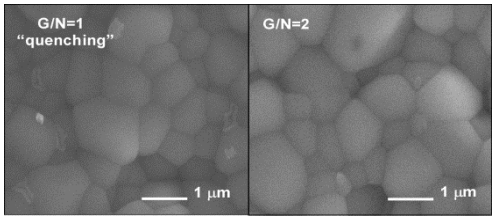

Figure 11

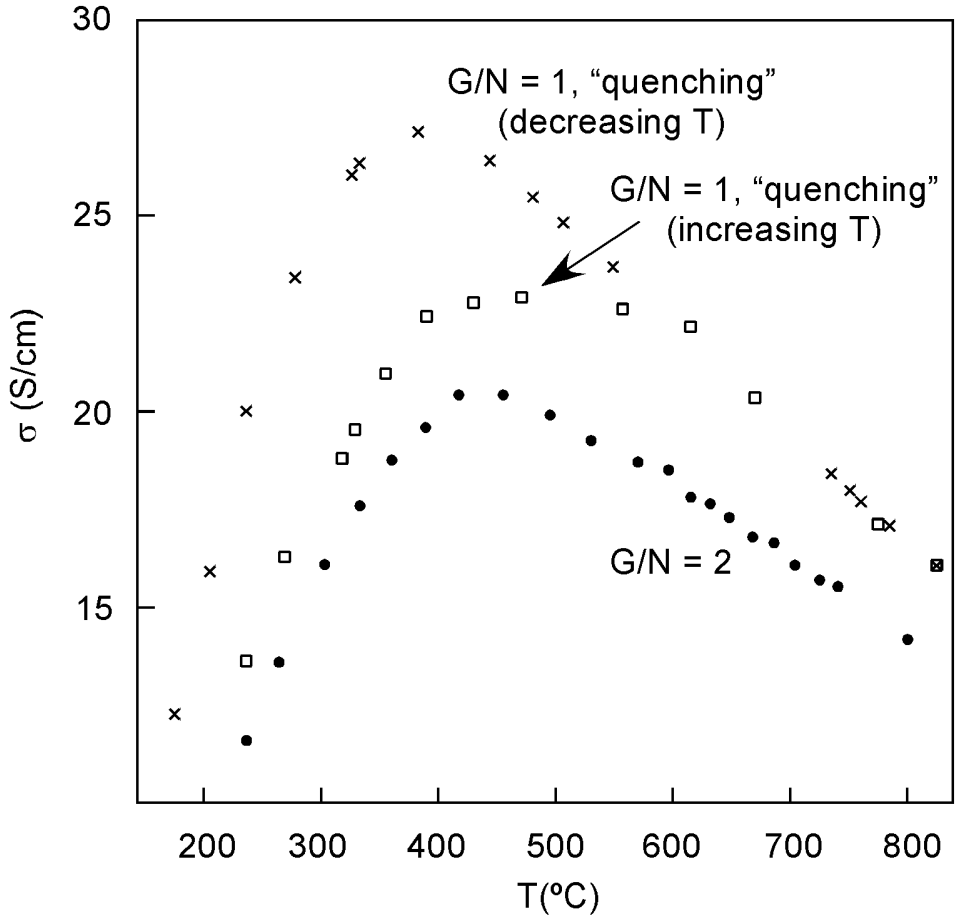

Figure 12

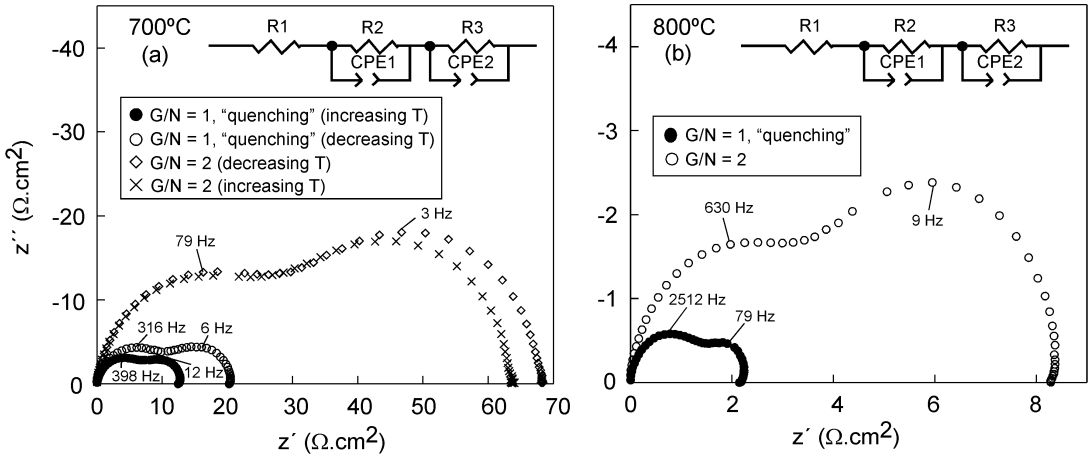

Figure 13

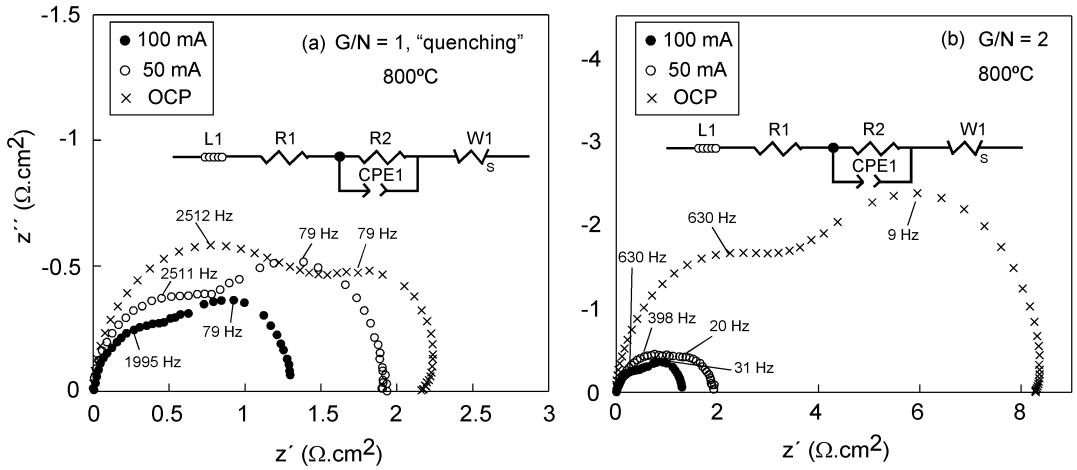

Graphical Abstract

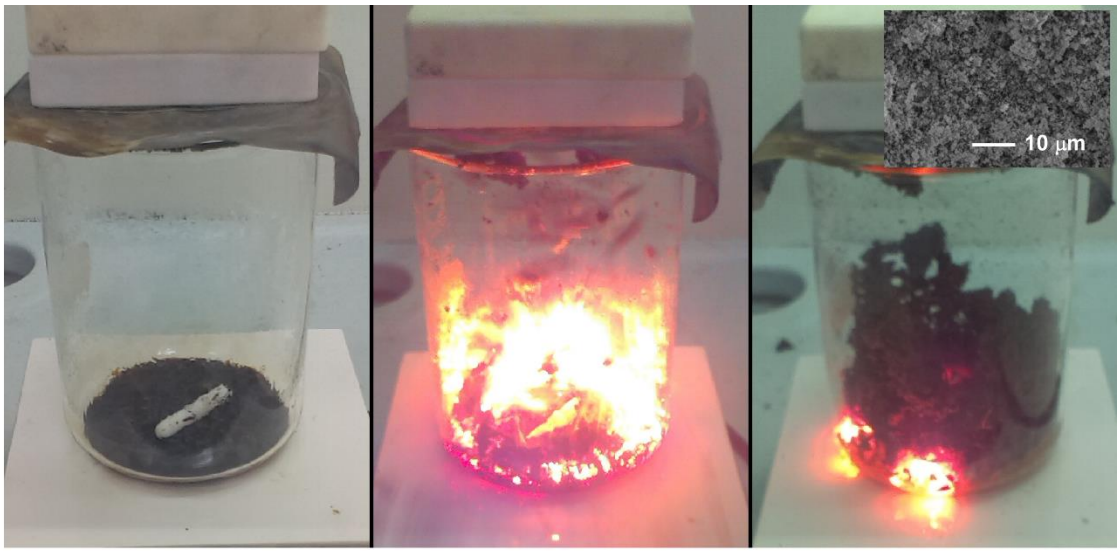

Calcination at 1200ºC

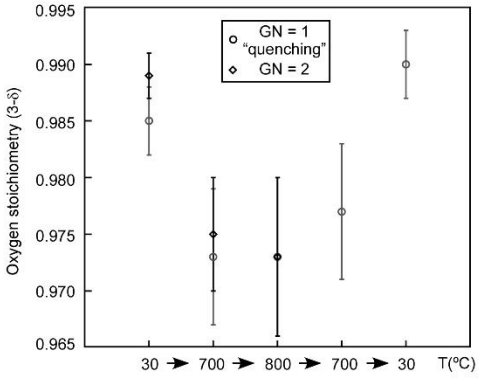

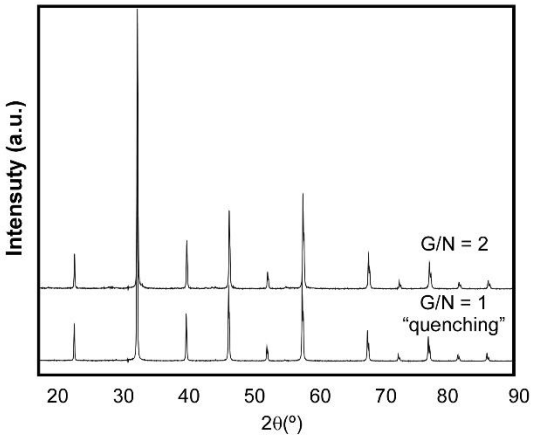

Highlights

The perovskite $La_{0.15}Sm_{0.35}Sr_{0.08}Ba_{0.42}FeO_{3-\delta}$ was prepared by the glycine-nitrate route.

Synchrotron powder diffraction data were collected from r.t. up to 800ºC in air.

The effect of the synthetic conditions on the electrochemical properties were analysed.